Insight on physical–mechanical properties of one-part alkali-activated materials based on volcanic deposits of Mt. Etna (Italy) and their durability against ageing tests

Claudio Finocchiaro · Germana Barone ⃝ **·**
Paolo Mazzoleni · Giuseppe Cultrone

Abstract In recent years, there has been a growing interest in one-part alkali-activated materials, which utilize solid-form alkali activators, within the construction industry. This approach is becoming popular due to its simpler and safer application for cast-in-situ purposes, as compared to the conventional two-part method. At this purpose, we have pioneered the use of volcanic deposits of Mt. Etna volcano (Italy) as precursor for the synthesis of a unique one-part formulation. This was done to assess its performance against both traditional and two-part alkali-activated materials. The study employed a comprehensive range of investigative techniques including X-ray powder diffraction, Fourier transform infrared spectroscopy, hydric tests, mercury intrusion porosimetry, ultrasound, infrared thermography, spectrophotometry, contact angle measurements, uniaxial compressive strength tests, as well as durability tests by salt crystallization and freeze–thaw cycles. The key findings on the studied samples are as follows: i) small size of pores and slow absorption-drying cycles; ii) satisfying compactness and uniaxial compressive strengths for building and restoration interventions;

iii) high hydrophily of the surfaces; iv) lower heating dispersion than traditional materials; v) significant damage at the end of the salt crystallization test; vi) excellent resistance to freeze–thaw cycles. These newly developed materials hold promises as environmentally friendly options for construction applications. They offer a simplified mixing process in contrast to the conventional two-part alkali-activated materials, thus providing an added advantage to this class of materials.

Keywords Volcanic deposits · One-part alkali-activated materials · Hydric and ageing tests · Porosimetry · Compressive strength

1 Introduction

The principles of environmental sustainability and circular economy, promoted by the European policy, push towards an ecological transition [1]. In particular, for the material sector the design of advanced materials with low CO_2 emissions that can be produced from natural or industrial waste sources is required to limit the depletion of natural resources [2]. In this context, alkali-activated materials (AAMs) present an eco-friendly alternative to conventional cement-based materials, which contribute to approximately 10% of global CO_2 emissions [3]. AAMs are solid materials synthesized by combining "two-parts": a powdered aluminosilicate source with an

C. Finocchiaro · G. Barone (✉) · P. Mazzoleni
Department of Biological, Geological and Environmental
Sciences, University of Catania, Catania, Italy
e-mail: gbarone@unict.it

G. Cultrone
Department of Mineralogy and Petrology, University
of Granada, Granada, Spain

alkaline solution, typically based on sodium (Na) or potassium (K) [4]. The main advantages of this class of materials include the possibility of using precursors from both natural wastes and industrial by-products, thus providing a sustainable approach to waste management [5], as well as the wide versatility for various industrial applications thanks to their favourable technological approach [6].

However, the use of concentrated aqueous alkali solutions, which are known for their corrosive nature makes less user-friendly and pose potential risks during material preparation and application. At this purpose, in the last years one-part or "just add water" alkali-activated materials (AAM) were designed and developed with high advantages in terms of logistics and adaptability to various scenarios [7]. This approach involves a dry mix, containing solid aluminosilicate precursor, solid alkali source and optional admixtures, triggered only by water, like for the preparation of ordinary Portland cement [8]. However, further researches on optimising mixes made from different precursors than fly deposits and blast furnace slag are required. Indeed, the few works in the literature aiming at characterizing one-part mixtures based on volcanic precursors, namely based on pumice coming from a mine in Idaho (United States) or volcanic deposits from Manisa (Turkey), have obtained satisfactory physical–mechanical properties, but without information on their durability [9, 10]. Moreover, a thermal treatment of the mixture at 60 °C for ten days was carried out for the curing of one-part mixtures based on volcanic deposits from Manisa (Turkey) [10].

The abundant deposits of volcanic deposits spread out worldwide represent a promising and natural waste resource with great potential to produce innovative and sustainable building materials [11, 12]. The chemical and mineralogical compositions of both fresh and aged volcanic deposits, exemplified by those from Mt. Etna volcano in Sicily (Italy), validate their suitability for the alkaline environment required for AAMs [13]. While these volcanic materials may benefit from the addition of a small amount of metakaolin to enhance aluminium availability and reactivity, previous research has already demonstrated their remarkable performance in terms of network reticulation, compressive strength, porosity and overall durability [14]. In particular, the choice of alkaline solution significantly influences the final

performance, with potassium-based solutions showing superior results compared to sodium-based alternatives both at room temperature and after thermal treatments up to 1000 °C [15]. Furthermore, AAMs based on volcanic sources have exhibited exceptional resistance to atmospheric exposure [16] and salt spray, making them particularly suitable for applications in coastal regions [17]. Their successful use in *in-situ* restoration works is exemplified by the restoration of a mosaic area in the UNESCO World Heritage Site, Monreale Cathedral in Sicily (Italy), highlighting the practical and beneficial use of volcanic-based AAMs in real-world restoration and construction activities [18].

In this work a set of one-part of AAMs based on volcanic deposits from Mt. Etna volcano (Italy) has been synthetized and, for the first time, thoroughly investigated in terms of mineralogy, physical–mechanical performance and durability to ageing tests, in order to compare their performance with those of two-parts and some traditional materials in order to find the most suitable applications and underline the advantages of one-part system.

2 Materials and methods

2.1 Sample preparation

Volcanic deposits (Va) were sampled in a landfill belonging to the territory of Zafferana Etnea, located in the eastern flank of Mt. Etna volcano (Sicily, Italy), where pyroclastic deposits of recent and past eruptions are stockpiled. They were subjected to wet grinding, following a drying step to obtain a particle size suitable for the alkaline activation process, and thus, to be used as main precursor for the design of one-part alkali-activated paste. Volcanic deposits of Mt. Etna volcano have been recently chemically and mineralogically analysed by Barone et al. [19]. Chemically, they contain: $SiO_2 = 49\%$; $Al_2O_3 = 16\%$, $Fe_2O_3 = 12\%$; $TiO_2 = 2\%$; $Na_2O = 3.5\%$; $K_2O = 2\%$; $CaO = 10.5\%$; $MgO = 4\%$, while the main mineralogical phases are plagioclase, augite, forsterite and titanomagnetite are, together with a considerable amount of volcanic glass (~70%). The solid activator is made by the combination of pellets of Na-hydroxide (97% purity) and powder of Na-silicate (code: 373908, provided by Carlo Erba Reagents

srl, Italy) with a molar ratio $SiO_2/Na_2O = 2$. A commercial metakaolin, ARGICAL™ M1000 (Imerys, France), was added as reactive powder, whose chemical composition is: $SiO_2 = 55\%$; $Al_2O_3 = 40\%$, $Fe_2O_3 = 1.4\%$; $TiO_2 = 1.5\%$; $Na_2O + K_2O = 0.8\%$; $CaO + MgO = 0.3\%$; and $LOI = 1\%$. Mineralogically, few amount of quartz (α-SiO_2), anatase (TiO_2), and muscovite $(KAl_2(Si_3Al)O_{10}(OH)_2)$ were identified by X-ray diffraction analysis [20]. The preparation of the one-part alkali-activated paste based on volcanic deposits (Vop) was carried out at room temperature. It consisted of a preliminary and manual mixing of all the solid components, namely volcanic deposits, metakaolin and activators, following the final one with the use of tap water for 5 min, then the filling into the cubic mould and a vibration step to remove air bubbles. The mix design of this one-part alkali-activated paste had the following amounts: 53 wt% of volcanic deposits, 13 wt% of metakaolin, 2 wt% of sodium hydroxide, 13 wt% of sodium silicate and 18 wt% of tap water. All samples were prepared in the shape of cubes with edges of approximately 4 cm, which were then cured for 28 days before being analysed.

2.2 Methods

Different techniques were selected to characterize for the first time one-part alkali-activated paste based on volcanic deposits of Mt. Etna volcano. The mineralogical and molecular structure was evaluated respectively by means of X-ray powder diffraction and Attenuated Total Reflectance Fourier Transform Infrared Spectroscopy in order to define the reaction mechanism induced by the solid precursors and activator in the one-part system. Moreover, the physical behaviour was assessed by hydric tests, porosimetry, ultrasound, colorimetry, infrared thermography and contact angle tests. The durability was estimated after the salt crystallization and freeze–thaw cycles. Finally, mechanical tests were also carried out, including flexural and uniaxial compressive strength to assess the mechanical performance.

2.2.1 X-ray powder diffraction

X-ray powder diffraction (XRPD) analyses were carried out on raw and synthetized materials using a Miniflex Rigaku instrument equipped with a Ni filter

and CuKα radiation generated at 40 kV and 15 mA. The measurements involved scanning the samples at a speed of 5º/min with a step size of 0.02º, covering the 2θ range from 5° to 65°. Qualitative and quantitative data obtained were processed using BGMN/Profex 5.0 software [21]. Rietveld refinement was performed after the addition of 2 wt% of a standard corundum powder (NIST code 676a) to enable the quantification of mineralogical phases and amorphous content [22]. The structures of specific phases were identified by referencing the BGMN database (accessible at http://www.bgmn.de/index.html). The quality of the refinement results was assessed through visual comparisons of observed and calculated patterns, as well as the calculation of discrepancy indices, including the weight profile R-factor. Values lower than 10% for the R-factor indicated satisfactory refinement outcomes [23].

2.2.2 ATR FT-IR analysis

The chemical and molecular composition of synthetized material was carried out by means of Attenuated Total Reflectance Fourier Transform Infrared Spectroscopy (ATR FT-IR), using a Jasco 6200 infrared spectrometer, which performed 30 scans per measurement in the range of 4000—400 cm^{-1} and a resolution of 2 cm^{-1}. Data were acquired by the SPECTRA MANAGER v2 software. Three replicas were carried out on the alkali-activated powder to obtain an average spectrum.

2.2.3 Mechanical strengths

Mechanical tests were carried out using a Controls UNIFRAME automatic compression testing machine, using a 10 kN load cell for flexural tests and a 50 kN load cell for compressive tests. For the flexural tests, three prisms measuring $2 \times 2x8$ cm^3 were used. The uniaxial compressive strength was defined from the six resulting samples of the flexural test, following the methodology described in UNI-EN 1015–11 standard [24].

2.2.4 Determination of the pore system

To assess the water behaviour, a series of hydric tests following the UNE-EN 13755 [25] and NORMAL 29/88 [26] standards in controlled

thermo-hygrometric conditions at 18 °C and 35% relative humidity were conducted on cubic samples. These tests included free water absorption (A_b), forced water absorption under vacuum (A_f) and drying. From these tests, several crucial parameters were determined, such as the degree of pore interconnection (A_x) [27], the drying index (D_i), apparent density (ρ_a), real density (ρ_r) and open porosity (P_o), in accordance with the RILEM standard [28]. For a more comprehensive view of the porous system of the AA-paste mercury intrusion porosimetry analysis (MIP) was carried out using a Micromeritics Autopore V 9600 porosimeter, examining the pore size distribution in the range 0.002–200 μm of a fragment of approximately 1 cm^3, which was oven dried at 70 ± 5 °C for 8 h prior to analysis. Open porosity (P_{oMIP}), specific surface area (SSA) and apparent and real densities (ρ_{aMIP} and ρ_{rMIP}) were also determined.

2.2.5 Non-destructive testing

2.2.5.1 Ultrasound   Ultrasound technique was chosen to assess the degree of compactness, using a Control 58-E4800 ultrasonic pulse velocity tester with transducers operating at a frequency of 54 kHz and having a circular surface area of 27 mm. To ensure continuous contact with the material surfaces, a water-based eco-gel was applied onto the transducers. P-wave propagation was measured on three cubic samples in the three perpendicular directions. The measurement was conducted following the guidelines outlined in the ASTM D2845 [29] standard and expressed in m/s. Furthermore, the structural anisotropy (ΔM) was determined using the following equation [29]:

$$\Delta M = \frac{V_{\max} - V_{\min}}{V_{\max}} * 100$$

where $V_{\max}$ and $V_{\min}$ are respectively the maximum and minimum velocities measured regardless of the measurement direction.

2.2.5.2 Spectrophotometry   Spectrophotometry was chosen to quantify the colour resulting from the mixing design of the sample set. The measurement protocol adhered to the UNI-EN 15886 standard [30], using a portable Konica Minolta CM-700d instrument for data acquisition. The analysis was carried out within the wavelength range of 400–700 nm, using CIE illu-

minant D65 that simulates daylight conditions with a colour temperature of 6504 K. A pulsed xenon lamp with a UV cut filter illuminated an 8 mm diameter circular region of the synthesized surface, considering a vision angle of 10°. Parameters such as lightness (L^*), chromatic coordinates (a^* and b^*), chroma (C^*) and hue angle ($h°$) were determined. The measurements were performed in both SCI (specular component included) and SCE (specular component excluded) modes, with three replicate measurements obtained for each sample.

2.2.5.3 Infrared thermography   In order to qualitatively assess the propagation of heat, an infrared (IR) thermography technique was used. This method entails the conversion of thermal radiation into electric signals, which are subsequently visualized as an image. To conduct the experiment, a FLIR T440 thermographic camera was used in a laboratory within controlled thermo-hygrometric condition of 25 °C and 50% relative humidity. The cubic samples were heated on a hot plate positioned 30 cm from the camera lens for 30 min at a temperature of 50 °C. The process involved capturing IR thermographic images at 30 s intervals, allowing for the observation of heat propagation across the surface of the sample. Additionally, the isotherm at 50 °C was marked to further assess the spread of heat.

2.2.5.4 Contact angle test   The sessile drop method using by means of an OCA system (Dataphysic Contact angle system, software SCA20, Filderstadt, Germany) was performed to estimate the static contact angles of a drop of ultrapure water over the material surface, defining its hydrophobic behaviour. A drop volume equal to 4 μL was used as liquid amount. The contact angle value was calculated considering the average of 6 measurements carried out in different spot analysis, 10 s after the drop deposition.

2.2.6 Ageing tests: salt crystallization and freeze–thaw cycles

Fifteen freeze–thaw and fifteen salt crystallization cycles using a 14% $Na_2SO_4 \times 10H_2O$ solution on three AAM samples were carried out according to UNE-EN 12371 [31] and UNE-EN 12370 [32] standards, respectively. The freeze–thaw cycles quantified the stress caused by the increase in the volume of water

in the pores due to freezing at temperatures below 0 °C. Instead, the salt crystallization test replicated the decay due to the dissolution and recrystallization of soluble salts within their porous systems. The decay of the samples was monitored daily, measuring their weight and registering the loss of fragments.

3 Results and discussion

3.1 X-ray powder diffraction

Mineralogical qualitative and quantitative results were plotted and listed respectively in Fig. 1 and Table 1. Volcanic deposits showed the typical composition of basalt rock, namely in decreasing amount order: plagioclase, augite, olivine and iron-oxide (i.e., Ti-magnetite). Moreover, quartz, muscovite/illite and chlorite were detected, possibly due to the contamination of the volcanic deposits in the sampled landfilled
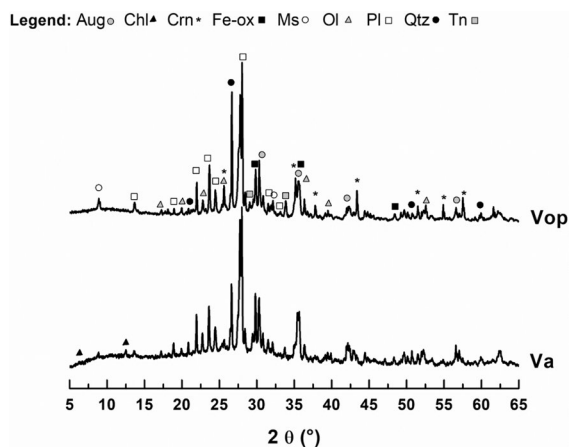
Fig. 1 XRPD pattern of raw material (Va) and synthetized paste (Vop). Mineral phases associated to the symbolism: Aug = augite; Chl = chlorite; Fe-ox = Ti-magnetite; Ms = muscovite; Ol = olivine; Pl = plagioclase; Qtz = quartz; Tn = trona. Mineral acronyms according to Whitney and Evans [38]

area [33]. This composition is almost equally balanced by the 57 wt.% of amorphous amount, whose value is strongly dependent to the fragmentation phenomena occurring during the eruption [34]. Contrary, the synthetized material (Vop) displayed a higher amorphous amount, 88 wt.%, in contraposition to a general decreasing of all mineral phases and the disappearance of chlorite due to the polycondensation reaction [35]. However, a secondary phase, namely trona $(Na_3(CO_3) \cdot (HCO_3) \cdot 2(H_2O))$, derived by the combination between the excess of unreacted Na^+ with CO_2 [19] was identified. This phenomenon is also common in other systems based on other volcanic precursors such as ghiara or pumice, both of which undergone to standard ageing or weathering conditions [36, 37]. Moreover, no mineralogical difference with the corresponding two-part system based on volcanic deposits from Mt. Etna volcano investigated in previous studies was observed.

3.2 ART FT-IR analysis

Notoriously, the alkali-activation process is extremely complex due to the several variables involved, leading to the sequence of different stages [39]. Figure 2 plotted the spectrum of the synthetized material obtained by ATR FT-IR for the understating of reaction mechanism of the system. The evidenced positions concern the stretching and bending of the O–H bonds at 3400 and 1640 cm^{-1}; the stretching vibrations of the O-C-O at 1400 cm^{-1}, suggesting the carbonation reaction between the carbon dioxide from the air and the free ions of the paste [40]; the asymmetric stretching vibrations of the Si–O-Si bonds at 1050 and 980 cm^{-1} [41]; the Si–O-Ca bond at 920 cm^{-1} [42], suggesting the formation of a Si–O-Ca co-network formed by the presence of free Ca ions released from the volcanic ash [15]. Therefore, according to the FT-IR results and the evidence found with XRPD, we supposed that the reaction was triggered by the metakaolin and the

Table 1 Mineralogical results (in wt.%) obtained by XRPD analysis with Rietveld Method. Aug = augite; Chl = chlorite; Fe-ox = Ti-mag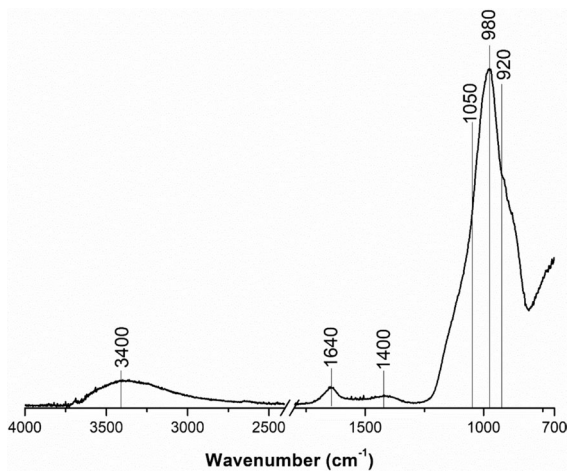netite; Ms = muscovite; Ol = olivine; Pl = plagi-oclase; Qtz = quartz; Tn = trona; amorph. = amorphous phase. Mineral acronyms according to Whitney and Evans [38]

	Aug	Chl	Fe-ox	Ms	Ol	Pl	Qtz	Tn	Amorph
Va	10.2	0.6	1.6	1.8	3.8	22.9	1.7	–	57.3
Vop	2.7	–	0.4	0.6	0.8	5.8	0.8	0.8	88.1

Fig. 2 – ATR FT-IR spectrum of synthetized paste collected in absorbance in the range of 4000–400 cm^{-1}. A break between 2400–1800 cm^{-1} was made for eliminating the atmospheric contribution

chemical reactants, which favour the increase of Si/Al species needed for the formation of the main network, thus balancing the low reactivity of the volcanic ash

at room temperature [43]. Moreover, the formation of another network based on Ca resulting from the partial dissolution of the Ca-species of volcanic ash (e.g., plagioclase and augite) was observed. Therefore, volcanic ash can be considered both as binder, because it partially participates in the reaction, and as a filler.

3.3 Mechanical strengths

In Table 2, flexural and uniaxial compressive average strengths were reported. In detail, the results showed a flexural resistance of 12 MPa ($\sigma = 1.3$) and a uniaxial compressive resistance of 27.4 MPa ($\sigma = 2.6$). These values are in agreement with those of previous works on two-parts AAMs based on volcanic deposits of Mt. Etna volcano (Italy), whose range is 15–40 MPa for the uniaxial compressive strengths [14, 17]. A slight reduction of 80 and 85% in compressive strengths in one-part system than two-parts AAMs was also observed by other authors [44]. This behaviour is probably due to the higher water content used to improve their lower workability (i.e., approximately 35% lower) [45]. Moreover, our average strengths are

Table 2 Physical and mechanical values. The standard deviation is indicated in brackets. Results obtained by hydric tests: A_b = free water absorption (%); A_f = forced water absorption (%); A_x = degree of pore interconnection (%); P_o = open porosity (%); ρ_a = apparent density (g/cm^3); ρ_r = real density (g/cm^3); D_i = drying index. Results obtained by MIP test: SSA = specific surface area (m^2/g); ρ_{rMIP} = real density (g/cm^3); ρ_{aMIP} = apparent density (g/cm^3); P_{oMIP} = open porosity (%). Results

obtained by ultrasound test: VP$_1$, VP$_2$, VP$_3$ = waves speed along the three orthogonal directions of cubic samples (m/s); ΔM = structural anisotropy (%). Results obtained by mechanical strength: S_{ux} = average uniaxial compressive strength (MPa); S_{fx} = average flexural strength (MPa). Results obtained by spectrophotometry: lightness (L*); chromatic coordinates (a* and b*); chroma (C*); hue angle (h°)

Hydric testes

A_b	A_f	A_x	P_o	ρ_a	ρ_r	D_i
7.09	8.69	18.60	15.57	1.79	2.12	0.941
(0.86)	(0.60)	(4.51)	(1.11)	(0.01)	(0.03)	(0.002)

Porosimetry

SSA	ρ_{rMIP}	ρ_{aMIP}	P_{oMIP}
23.5	2.51	2	20.52

Ultrasound

VP$_1$	VP$_2$	VP$_3$	VP$_4$	ΔM
2475.9	2421.3	2484.4	2460.5	5.2
			(34.24)	

Mechanical strengths

S_{ux}	S_{fx}
27.40	11.96
(2.59)	(1.25)

Spectrophotometry

L*	a*	b*	C*	h°
38.0	0.8	3.7	3.8	79.1
(4.3)	(0.3)	(0.6)	(0.7)	(3.0)

higher than one–part geopolymers obtained from the volcanic deposits from Manisa (Turkey), whose values range from 13.89 MPa to 19.6 MPa, despite the curing was at 60 °C for ten days [10]. Therefore, in general our one-part AAMs set achieved satisfactory resistance, especially for unstructured building or restoration fields.

### 3.4 Determination of the pore system

Figure 3 and Table 2 showed the main results concerning the hydric (a) and MIP (b) tests. In detail, the sample had a slow and little free water absorption capacity with a low percentage value (around 7% in the step 1 of Fig. 3a), whose value agree with the range (i.e., 7–16% in one-part alkali-activated blast furnace slag) found by Abdel-Gawwad and Abo-El-Enein [46], maybe due to the formation of hydration products and thus decreasing porosity. During forced water absorption (step 2 of Fig. 3a), the set showed an abrupt slope of the curve suggesting the difficulty of water circulation in the pore network [47]. This is confirmed by the high Ax value (~19%, Table 2) when compared with other construction materials (i.e., Ax values < 5 for bricks containing volcanic deposits from Mt. Etna volcano [48]). The poor interconnection between the pores caused a very slow drying ($D_i < 1\%$, Table 2), whose initial dry weight was not fully achieved even after about three weeks (step 3 of Fig. 3a). This phenomenon may be due to an interaction between the matrix sample and the water, leading to the formation of a gel-like substance within the pores, hindering the drying process or also due to the formation of trona within the pore network already identified by XPRD. The hydric behaviour determined an open porosity of ~16%, while the calculated values of apparent and real densities correspond to 1.8 and 2.1 g/cm^3, respectively. These values agree with those obtained by MIP test, although the latter are a slightly higher. The obtained results are consistent with those obtained in previous works where two-part AAMs based on volcanic deposits of Mt. Etna volcano were investigated [17, 19, 49] whose recorded values ranged between 1.9–2 g/cm^3 for real density and 24–26% for open porosity. However, the manufacturing process of our one-part AAMs increased the density and decreased the open porosity, suggesting a more compactness structure than the traditional two-parts AAMs. The MIP results evidenced a unimodal pore size distribution with the main peak ranged between 0.01 and 0.1 μm (Fig. 3b), which is in agreement with previous researches [19, 49].

3.5 Non-destructive testing

3.5.1 Ultrasound

Ultrasound usually give interesting features on compactness of the materials, which in turn depends on the own microstructure, namely mineralogy, density and porosity network [50–52]. Our results display an
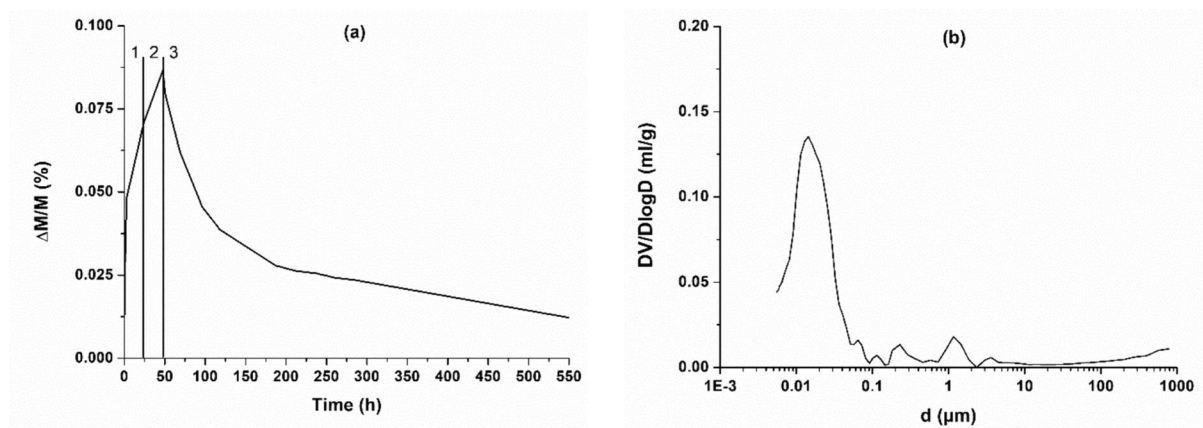
Fig. 3 Pore system evaluated by hydric (a) and MIP (b) testes: (a) Weight variation (ΔM/M%) versus time (in hours), whose trend is made of: 1) water absorption at atmospheric pressure, 2) water absorption under vacuum and 3) drying; (b) pore size distribution results: DV/DlogD (in ml/g) versus pore diameter (d, in μm)

average velocity of 2461 m/s (Table 2), which is in accordance with the range, 1500–3000 m/s, found in the literature on fly deposits-geopolymers differentiated by several concentrations of the alkali activator used [53]. Indeed, the concentration of alkali as well as the ratio between the alkaline solids to metakaolin generally influence the values of compactness as demonstrated by Albidah et al. [54], whose values agree with ours. Instead, the traditional cement concrete showed a higher compactness, depending to the water/cement ratio (w/c), whose range is 2800–4800 m/s [55]. Therefore, our synthetic materials have better insulating properties than traditional ones and this behaviour match with the natural stones. In fact, our sample set seems to have a compactness similar to sedimentary rocks, such as sandstone (1400–4200 m/s), limestone (2500–6000 m/s) and conglomerate (2500–5000 m/s) [56]. However, these rocks do not match with the mineralogy of our samples, not only because of the difference in minerals but especially for the amorphous and semi-crystalline microstructure which differs from that of sedimentary rocks. In fact, the ultrasound velocity in glassy materials is, generally, attenuated compared to crystalline ones [57].

3.5.2 Spectrophotometry

The colorimetric results confirmed the negative correlation between the high concentration of volcanic deposits, used as main precursor in our alkaline system, with the lightness (L*, Table 2). Indeed, this latter is low, mostly uniform in all surfaces. Moreover, also the chromatic parameters, a* and b*, have very low values, lying within the greyish chroma (C*, Table 2). These chromatic values are in accordance with those obtained by Occhipinti et al. [36] on two-parts AAMs based on volcanic deposits investigated before and after weathering exposition. However, slight difference in terms of lightness was recorded, probably due to the different alkaline synthesis approach (i.e., two-part).

3.5.3 Infrared thermography

Figure 4 showed the IR images of the sample respectively at 2 min and 30 min of heating. The heating spread homogeneously from the bottom to the top. In detail, during the first two minutes, the thermal absorption was gradual, reaching an average temperature of about 35 °C within the first few millimetres (Fig. 4a). Instead, the isotherm at 50 °C recorded at the end of the test was marked at 13 mm from the bottom, meaning a 35.5% of the sample surface (Fig. 4b). Notoriously, the thermal conductivity of a ceramic material, traditional or advanced like geopolymer [58], is subject to various influencing factors such as the mineralogical composition, moisture content, grain size of the raw material, as well as the apparent density, porosity and pore size distribution, which
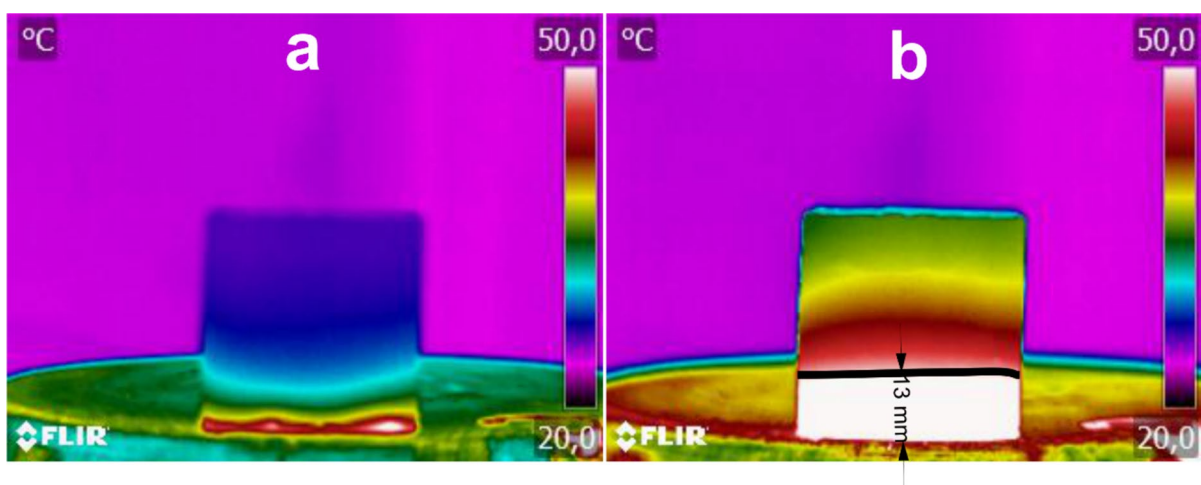
Fig. 4 - IR-thermographic images took after 2 min (a) and 30 min of eating; the continuous line marks the 50 °C isotherm (b). The images were configured with the lava palette colours
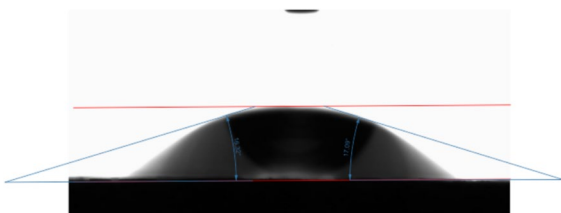
play a significant role [59, 60]. Moreover, another work, based on the estimation of heat dispersion, demonstrated the potential of IR-thermography to derive indirect information on the physical–mechanical behaviour of two-part alkali activated materials based on volcanic deposits [17].
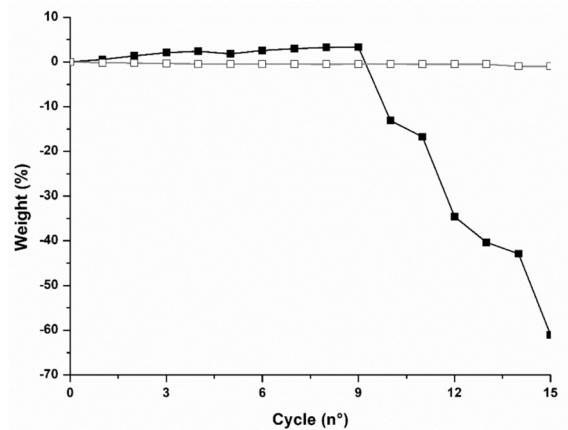
Comparing the isotherms at 50 °C of our sample set with those of traditional ceramics studied using the same setting measurement [50], the heat absorption rate of our one-part AAMs was significantly lower than that of traditional materials. Therefore, this behaviour confirms the potential application of alkali activated materials for high thermal insulation applications [61].

3.5.4 Contact angle test

The contact angle is considered a measure of hydrophobicity of the surface. The absorption rate of drop water used for the test was very fast. Indeed, the recorded average angle value at time t_0 was of 18.20° (st. 0.64), corresponding to the instantaneous contact between the drop and the surface (Fig. 5). Therefore, there was no evolution during the 10 s because the absorption was immediate: typical behaviour of hydrophilic surfaces [62]. Similar behaviour has been observed when analysing the surface of cement-based mortars, whose results were ranging between 22° and 26° at t_0 [63]. In view of this, these synthetized materials should be used for indoor applications or for outdoor environments based on a pre-treatment with waterproofing coatings in order to enhance the hydrophobicity [64].

Fig. 6 Weight variations over 15 salt crystallization (black) and freeze–thaw (grey) cycles. Each curve represents the mean of three measurements

3.6 Ageing tests: salt crystallization and freeze–thaw cycles

The weight loss after the salt crystallization cycles were plotted in Fig. 6. Specifically, the sample evidenced a mass loss of 60 wt% at the end of the test. The damages start at the edges and corners, where tiny fragments separate from the cubic samples preserving their core. Therefore, the salt crystallization cycles produced significant damage at the end of the test. This behaviour is very interesting considering the low porosity and unimodal pore size of the matrix, which normally have a negative effect on the material's durability to salt crystallization [65]. Differently, one-part geopolymer synthesized by calcium carbide residue-sodium carbonate-activation of slag showed limited sodium sulphate degradation [66]. Moreover, the resistance to salt crystallization is strongly influenced by the calcium content of the precursors and cross linked aluminosilicate gel, which can lead to the formation of gypsum or ettringite [67]. The sample performs much better to freeze–thaw compared to salt crystallization (Fig. 6). In fact, during the fifteen cycles the material recorded a very little weight loss (< 1%). This result agrees with the very low weight loss (i.e., around 2% after 15 cycles at − 5 °C) recorded in similar materials [68], confirming the high resistance to freezing. However, the weight loss increases with decreasing the freezing temperature,

Fig. 5 – Representative measurement of contact angle at time t_0 of our sample

increasing the number of cycles and also depending on the activator used [68]. According to the results of ageing tests performed, this class of material is suitable for applications in cold $(> -5\ °C)$ coastal environments [69].

4 Conclusions

The proposed methodological approach was useful to define the microstructural features of one-part alkali-activated materials to assess their decay behaviour. Indeed, the obtained results highlight the coexistence of Si–O-Si and Si–O-Ca networks for the contribution of volcanic ash both in the reaction mechanism and as filler in the mixture. Moreover, this latter is characterized by a small size of pores, confirmed, also, by the slow absorption-drying rates recorded during the hydric tests. This behaviour can be due to the interaction of the matrix sample and water causing the formation of trona or a gel in the pores, which hampers the drying. Ageing tests showed poor resistance to salt crystallization but excellent durability to freezing, suggesting applications in cold coastal environments. Moreover, the compactness and uniaxial compressive strength are satisfactory for building and restoration interventions, although outdoor applications are not recommended due to the high hydrophily of the surfaces if these latter are not pre-treated with specific coatings. On the other hand, they showed slow heat propagation, making them a viable alternative for thermal insulation properties. Therefore, these synthetized materials can represent a potential eco-friendly material for building applications with a simplified mixing procedure contrary to the common two-part AAMs, representing an adding value for this material class.

Author contributions All authors contributed to the study conception, once idealized by Claudio Finocchiaro. Material preparation, data collection and analysis were performed by Claudio Finocchiaro. The first draft of the manuscript was written by Claudio Finocchiaro and supervised by Giuseppe Cultrone, Germana Barone and Paolo Mazzoleni. All authors read and approved the final manuscript.

Declarations

Conflict of interests The authors declare that they have no conflict of interest.

References

1. Arora NK, Mishra I (2019) United nations sustainable development goals 2030 and environmental sustainability: race against time. Environmental Sustainability, 2(4) 339–342. https://doi.org/10.1007/S42398-019-00092-Y

2. Brilha J, Gray M, Pereira DI, Pereira P (2018) Geodiversity: an integrative review as a contribution to the sustainable management of the whole of nature. Environ Sci Policy 86:19–28. https://doi.org/10.1016/J.ENVSCI.2018.05.001

3. Belaïd F (2022) How does concrete and cement industry transformation contribute to mitigating climate change challenges? Resources. Conservation Recycling Adv 15:200084. https://doi.org/10.1016/J.RCRADV.2022.200084

4. Pacheco-Torgal F, Labrincha JA, Leonelli C et al (2014) Handbook of alkali-activated cements Mortars and Concretes. Elsevier Inc

5. Provis JL (2018) Alkali-activated materials. Cem Concr Res 114:40–48. https://doi.org/10.1016/J.CEMCONRES.2017.02.009

6. He P, Jia D, Wang S (2013) Microstructure and integrity of leucite ceramic derived from potassium-based geopolymer precursor. J Eur Ceram Soc 33:689–698. https://doi.org/10.1016/J.JEURCERAMSOC.2012.10.019

7. Luukkonen T, Abdollahnejad Z, Yliniemi J et al (2018) One-part alkali-activated materials: a review. Cem Concr Res 103:21–34. https://doi.org/10.1016/j.cemconres.2017.10.001

8. Elzeadani M, Bompa DV, Elghazouli AY (2022) One part alkali activated materials: a state-of-the-art review. J Build Eng 57:104871. https://doi.org/10.1016/J.JOBE.2022.104871

9. Almalkawi AT, Hamadna S, Soroushian P (2017) One-part alkali activated cement based volcanic pumice. Constr Build Mater 152:367–374. https://doi.org/10.1016/j.conbuildmat.2017.06.139

10. Çetintaş R, Soyer-Uzun S (2018) Relations between structural characteristics and compressive strength in volcanic ash based one–part geopolymer systems. J Build Eng 20:130–136. https://doi.org/10.1016/J.JOBE.2018.07.011

11. Mañosa J, Serrano-Conte J, Maldonado-Alameda A et al (2023) Pyroclastic volcanic ash as a potential precursor of alkali-activated binders – a case study from Tajogaite (La Palma, Canary Islands) volcano eruption. J Build Eng 72:106623. https://doi.org/10.1016/J.JOBE.2023.106623

12. Cavalieri M, Ferrara PL, Finocchiaro C, Martorana MF (2024) An economic analysis of the use of local natural waste: volcanic ash of Mt. etna volcano (Italy) for geopolymer production. Sustainability 16:740. https://doi.org/10.3390/SU16020740

13. Lanzafame G, Caggiani MC, Finocchiaro C, et al (2022) Multidisciplinary characterization of the "Ghiara" volcanic paleosoil (Mt. Etna volcano, Italy): Petrologic characters and genetic model. Lithos 418–419:106679. https://doi.org/10.1016/J.LITHOS.2022.106679

14. Finocchiaro C, Barone G, Mazzoleni P, Sgarlata, Caterina Lancellotti, Isabella Leonelli, Cristina, Romagnoli M (2021) Artificial Neural Networks Test for the Prediction of Chemical Stability of Pyroclastic Deposits-Based AAMs and Comparison with Conventional Mathematical Approach (MLR). J Mater Sci 56: 513–527. https://doi.org/10.1007/s10853-020-05250-w

15. Scanferla P, Finocchiaro C, Gharzouni A, et al (2023) High temperature behavior of sodium and potassium volcanic ashes-based alkali-activated materials (Mt. Etna, Italy). Constr Build Mater 408:133702. https://doi.org/10.1016/J.CONBUILDMAT.2023.133702

16. Occhipinti R, Caggiani MC, de Ferri L et al (2023) Structural properties of volcanic precursors-based geopolymers before and after natural weathering. Ceram Int 49:21892–21902. https://doi.org/10.1016/J.CERAMINT.2023.04.013

17. Finocchiaro C, Belfiore CM, Barone G, Mazzoleni P (2022) IR-Thermography as a non-destructive tool to derive indirect information on the physical-mechanical behaviour of alkali activated materials. Ceram Int. https://doi.org/10.1016/J.CERAMINT.2022.08.174

18. Fugazzotto M, Occhipinti R, Cristina Caggiani M, et al (2023) Restoration feasibility study by using alkali activated mortars based on Mt. Etna volcanic ash: The case study of Monreale Cathedral (Palermo, Italy). Mater Lett 333:133626. https://doi.org/10.1016/J.MATLET.2022.133626

19. Barone G, Finocchiaro C, Lancellotti I et al (2021) Potentiality of the use of pyroclastic volcanic residues in the production of alkali activated material. Waste Biomass Valorization 12:1075–1094. https://doi.org/10.1007/s12649-020-01004-6

20. Finocchiaro C, Occhipinti R, Barone G et al (2024) Effects of the addition of slaked lime to alkali-activated pastes based on volcanic ashes from Mt. Etna volcano (Italy). Ceram Int 50:24479–24486. https://doi.org/10.1016/J.CERAMINT.2024.04.181

21. Doebelin N, Kleeberg R (2015) Profex: a graphical user interface for the rietveld refinement program BGMN. J Appl Crystallogr 48:1573–1580. https://doi.org/10.1107/S1600576715014685/HTTPS://JOURNALS.IUCR.ORG/SERVICES/RSS.HTML

22. Gualtieri AF, Zanni M (1998) Quantitative determination of crystalline and amorphous phase in traditional ceramics by combined rietveld-RIR method. Mater Sci Forum 278–281:834–839. https://doi.org/10.4028/www.scientific.net/MSF.278-281.834

23. Nguyen D-C, Chu C-C, Anbalagan AK, et al (2021) Rietveld Refinement and X-ray Absorption Study on the Bonding States of Lanthanum-Based Perovskite-Type Oxides La1− xCexCoO3. Crystals 12:50. https://doi.org/10.3390/CRYST12010050

24. EN 1015–11 (2019) Methods of test for mortar for masonry - Part 11: Determination of flexural and compressive strength of hardened mortar

25. UNI-EN 13755 (2008) Natural Stone Test Methods. Determination of Water Absorption at Atmospheric Pressure

26. NORMAL 29/88 (1988) Misura dell'indice di asciugamento (drying index)

27. Cultrone G, De La Torre MJ, Sebastián E, Cazalla O (2003) Evaluation of bricks durability using destructive and nondestructive methods (DT and NDT). Mater Constr 53:41–60. https://doi.org/10.3989/MC.2003.V53.I269.267

28. Rilem (1980) Recommended test to measure the deterioration of stone and to assess the differences of treatment methods. Mater Struct 13:175–253

29. ASTM D (2005) Standard test method for laboratory determination of pulse velocities and ultrasonic elastic constant of rock

30. UNE-EN 15886 (2011), Conservation of Cultural Property. Test Methods. Colour Measurement of Surfaces. Madrid, Spain

31. UNE-EN 12371 2011 Metodos de ensayo para piedra natural. Determinacion de la resistencia a la heladicidad, Madrid

32. UNI-EN 12370 (2020) Natural Stone Test Methods. Determination of Resistance to Salt Crystallization

33. Shen M, Dai S, Graham IT et al (2021) Mineralogical and geochemical characteristics of altered volcanic ashes (tonsteins and K-bentonites) from the latest Permian coal-bearing strata of western Guizhou Province, southwestern China. Int J Coal Geol 237:103707. https://doi.org/10.1016/J.COAL.2021.103707

34. Barone G, Mazzoleni P, Corsaro RA et al (2016) Nanoscale surface modification of Mt Etna volcanic ashes. Geochim Cosmochim Acta 174:70–84. https://doi.org/10.1016/j.gca.2015.11.011

35. Nikolov A, Rostovsky I, Nugteren H (2017) Geopolymer materials based on natural zeolite. Case Stud Constr Mater 6:198–205. https://doi.org/10.1016/j.cscm.2017.03.001

36. Occhipinti R, Caggiani MC, Andriulo F et al (2022) Effect of atmospheric exposure on alkali activated binders and mortars from Mt Etna volcanic precursors. Mater Lett 315:131940. https://doi.org/10.1016/j.matlet.2022.131940

37. Occhipinti R, Stroscio A, Finocchiaro C et al (2020) Alkali activated materials using pumice from the aeolian islands (sicily, italy) and their potentiality for cultural heritage applications: preliminary study. Constr Build Mater 259:120391. https://doi.org/10.1016/j.conbuildmat.2020.120391

38. Whitney DL, Evans BW (2010) Abbreviations for names of rock-forming minerals. Am Miner 95:185–187. https://doi.org/10.2138/AM.2010.3371

39. Sun B, Ye G, de Schutter G (2022) A review: reaction mechanism and strength of slag and fly ash-based alkali-activated materials. Constr Build Mater 326:126843. https://doi.org/10.1016/J.CONBUILDMAT.2022.126843

40. Peyne J, Gautron J, Doudeau J et al (2017) Influence of calcium addition on calcined brick clay based geopolymers: a thermal and FTIR spectroscopy study. Constr Build Mater 152:794–803. https://doi.org/10.1016/J.CONBUILDMAT.2017.07.047

41. Scanferla P, Gharzouni A, Texier-Mandoki N et al (2023) Polycondensation reaction effect on the thermal behavior of metakaolin-based potassium geopolymers. J Sol-Gel Sci Technol 2023:1–14. https://doi.org/10.1007/S10971-023-06080-3

42. Gharzouni A, Ouamara L, Sobrados I, Rossignol S (2018) Alkali-activated materials from different aluminosilicate sources: effect of aluminum and calcium availability. J Non Cryst Solids 484:14–25. https://doi.org/10.1016/J.JNONCRYSOL.2018.01.014

43. Djobo JNY, Elimbi A, Tchakouté HK, Kumar S (2016) Reactivity of volcanic ash in alkaline medium, microstructural and strength characteristics of resulting geopolymers under different synthesis conditions. J Mater Sci 51:10301–10317. https://doi.org/10.1007/s10853-016-0257-1

44. Segura IP, Luukkonen T, Yliniemi J et al (2022) Comparison of one-part and two-part alkali-activated metakaolin and blast furnace slag. J Sustain Metall 8:1816–1830. https://doi.org/10.1007/S40831-022-00606-9/FIGURES/11

45. Nematollahi B, Sanjayan J, Shaikh FUA (2015) Synthesis of heat and ambient cured one-part geopolymer mixes with different grades of sodium silicate. Ceram Int 41:5696–5704. https://doi.org/10.1016/J.CERAMINT.2014.12.154

46. Abdel-Gawwad HA, Abo-El-Enein SA (2016) A novel method to produce dry geopolymer cement powder. HBRC J 12:13–24. https://doi.org/10.1016/J.HBRCJ.2014.06.008

47. Hall C, Hoff WD (2009) Water transport in brick, stone and concrete, second edition, 3th ed

48. Cultrone G (2022) The use of Mount Etna volcanic ash in the production of bricks with good physical-mechanical performance: converting a problematic waste product into a resource for the construction industry. Ceram Int 48:5724–5736. https://doi.org/10.1016/J.CERAMINT.2021.11.119

49. Finocchiaro C, Barone G, Mazzoleni P, et al (2020) FT-IR study of early stages of alkali activated materials based on pyroclastic deposits (Mt. Etna, Sicily, Italy) using two different alkaline solutions. Constr Build Mater 262:120095. https://doi.org/10.1016/j.conbuildmat.2020.120095

50. Cultrone G, Aurrekoetxea I, Casado C, Arizzi A (2020) Sawdust recycling in the production of lightweight bricks: how the amount of additive and the firing temperature influence the physical properties of the bricks. Constr Build Mater 235:117436. https://doi.org/10.1016/J.CONBUILDMAT.2019.117436

51. Jamshidi A, Zamanian H, Zarei Sahamieh R (2018) The effect of density and porosity on the correlation between uniaxial compressive strength and P-wave velocity. Rock Mech Rock Eng 51:1279–1286. https://doi.org/10.1007/S00603-017-1379-8/FIGURES/6

52. Zhang X, Baudet BA, Yao T (2020) The influence of particle shape and mineralogy on the particle strength, breakage and compressibility. Int J Geo-Eng 11:1–10. https://doi.org/10.1186/S40703-020-0108-4/FIGURES/7

53. Ghosh R, Sagar SP, Kumar A et al (2018) Estimation of geopolymer concrete strength from ultrasonic pulse velocity (UPV) using high power pulser. J Build Eng 16:39–44. https://doi.org/10.1016/J.JOBE.2017.12.009

54. Albidah A, Alghannam M, Abbas H et al (2021) Characteristics of metakaolin-based geopolymer concrete for different mix design parameters. J Market Res 10:84–98. https://doi.org/10.1016/J.JMRT.2020.11.104

55. Jiang J, Zhang D, Gong F, Zhi D (2022) Prediction of ultrasonic pulse velocity for cement, mortar, and concrete through a multiscale homogenization approach. Materials. https://doi.org/10.3390/MA15093241

56. González de Vallejo L (2002) Ingeniería geológica. Prentice Hall

57. Ghosh US (1995) Ultrasonic velocity and attenuation in glass. Bull Mater Sci 18:61–73. https://doi.org/10.1007/BF02745271/METRICS

58. Davidovits J (2017) Geopolymers: Ceramic-like inorganic polymers. J Ceramic Sci Technol 8:335–350. https://doi.org/10.4416/JCST2017-00038

59. Gualtieri ML, Gualtieri AF, Gagliardi S et al (2010) Thermal conductivity of fired clays: Effects of mineralogical and physical properties of the raw materials. Appl Clay Sci 49:269–275. https://doi.org/10.1016/J.CLAY.2010.06.002

60. Šveda M, Janík B, Pavlík V et al (2017) Pore-size distribution effects on the thermal conductivity of the fired clay body from lightweight bricks. J Build Phys 41:78–94. https://doi.org/10.1177/1744259116672437/ASSET/IMAGES/LARGE/10.1177_1744259116672437-FIG14.JPEG

61. Lahoti M, Tan KH, Yang EH (2019) A critical review of geopolymer properties for structural fire-resistance applications. Constr Build Mater 221:514–526. https://doi.org/10.1016/J.CONBUILDMAT.2019.06.076

62. Drelich J, Chibowski E, Meng DD, Terpilowski K (2011) Hydrophilic and superhydrophilic surfaces and materials. Soft Matter 7:9804–9828. https://doi.org/10.1039/C1SM05849E

63. Klein NS, Bachmann J, Aguado A, Toralles-Carbonari B (2012) Evaluation of the wettability of mortar component granular materials through contact angle measurements. Cem Concr Res 42:1611–1620. https://doi.org/10.1016/J.CEMCONRES.2012.09.001

64. Ma J, Porath LE, Haque MF, et al (2021) Ultra-thin self-healing vitrimer coatings for durable hydrophobicity. Nature Communications, https://doi.org/10.1038/s41467-021-25508-4

65. Scherer GW (1999) Crystallization in pores. Cem Concr Res 29:1347–1358. https://doi.org/10.1016/S0008-8846(99)00002-2

66. Yang T, Gao X, Zhang J et al (2022) Sulphate resistance of one-part geopolymer synthesized by calcium carbide residue-sodium carbonate-activation of slag. Compos B Eng 242:110024. https://doi.org/10.1016/J.COMPOSITESB.2022.110024

67. Kuri JC, Nuruzzaman M, Sarker PK (2023) Sodium sulphate resistance of geopolymer mortar produced using ground ferronickel slag with fly ash. Ceram Int 49:2765–2773. https://doi.org/10.1016/J.CERAMINT.2022.09.258

68. Min Y, Wu J, Li B et al (2022) Experimental study of freeze–thaw resistance of a one-part geopolymer paste. Case Stud Constr Mater 17:e01269. https://doi.org/10.1016/J.CSCM.2022.E01269

69. Jin M, Wang Z, Lian F, Zhao P (2020) Freeze-thaw resistance and seawater corrosion resistance of optimized tannery sludge/metakaolin-based geopolymer. Constr Build Mater 265:120730. https://doi.org/10.1016/J.CONBUILDMAT.2020.120730